Nanoscale

PAPER

View Article Online
View Journal | View Issue

Check for updates

Cite this: *Nanoscale*, 2026, **18**, 2780

Strain control of the electronic structure in WS_2 homobilayers with 0° and 60° stacking angles

Valentino Jadriško, *[a] Irantzu Landa-Garcia,[a] Dino Novko,[b] Borna Radatović,[c] Qianjie Lei,[d] Nataša Vujičić,[b] Christoph Gadermaier,[a] Andres Castellanos-Gomez[e] and Yong Xie[d,e]

Received 7th May 2025,
Accepted 21st November 2025

DOI: 10.1039/d5nr01872b

rsc.li/nanoscale

Two-dimensional transition metal dichalcogenides combine attractive semiconductor properties with exceptionally strong light–matter interaction. Their mechanical robustness allows the modulation of their optical and electronic functionalities *via* strain. Bilayers introduce the stacking angle as an additional parameter, whose role in the strain response is still elusive. Here, we combine differential reflectance spectroscopy and density functional theory calculations to explore the strain response of WS_2 homobilayers with 0° and 60° stacking angles. The change of the excitonic resonance energies and linewidths depends on the stacking angle, highlighting the scope for the manipulation of the electronic structure of two-dimensional semiconductors *via* the synergistic harnessing of the strain and angle control parameters.

Introduction

Two-dimensional transition metal dichalcogenides (TMDCs) combine attractive semiconductor properties and mechanical and chemical robustness with exceptionally strong light–matter interaction. As evidence of this, TMDC monolayers with sub-nanometer thickness have demonstrated a range of optical phenomena, including photodetection,[1] photovoltaics,[2] saturable absorption,[3] optical gain,[4] photocatalysis,[5] electrooptical modulation,[6] and optical parametric amplification.[7]

Strain can significantly modulate the band structure of TMDCs,[8–19] resulting in a red-shift of the excitonic resonances by several tens of meV per % of uniaxial strain[8–23] and, in some cases, inducing a crossover between direct and indirect semiconductor behavior.[10,13,16] Moreover, strain also influences the strength of the electron–phonon coupling,[24–28] resulting in a variation in the spectral linewidth of the exciton features and charge carrier mobility.[29–32]

Experimental investigation of TMDCs' optical properties under strain has so far been largely limited to monolayer material. In bilayer TMDCs, the second atomic layer commonly adopts specific stacking orientations, such as 0° rotation or 60° rotation, due to their enhanced thermodynamic stability compared to other possible configurations.[33] The few existing works on bilayer material have found direct-to-indirect bandgap transitions,[13,14,16,25,34] a change in the exciton-phonon coupling[35] and a modulation of the Stokes shift.[36] None of the existing studies has yet assessed the role of the interlayer stacking angle in the strain response.

Here, we study the strain tunable optical properties of WS_2 homobilayers in 0° and 60° stacking configurations through combination of differential reflectance contrast (DR) and density functional theory (DFT) calculations. Experiments and calculations yield consistent linear strain gauge factors (GFs) that are slightly higher for the A exciton compared to the B exciton. Additionally, the measured strain GFs are about 25% higher for 60° stacking relative to 0° stacking. Our results are a first step toward a synergistic use of strain and stacking in the modulation of the electronic structures of two-dimensional semiconductors.

Methods

The WS_2 bilayer flakes were grown using a modified one-zone chemical vapor deposition process, as shown in our previous reports.[33,37,38] First, the metal source WO_3 powder (Alfa Aesar, 99.8%) was loaded into the boat with the SiO_2/Si substrate facing the source materials. The source boat was placed at the center part of the growth furnace. Then, the sulfur powder was loaded onto the edge of the furnace with a movable inner tube and heated above 100 °C for more than 15 min to eliminate

[a]*Dipartimento di Fisica, Politecnico di Milano, Piazza Leonardo da Vinci 32, 20133 Milano, Italy. E-mail: valentino.jadrisko@polimi.it*
[b]*Center for Advanced Laser Techniques, Institute of Physics, Bijenička 46, 10000 Zagreb, Croatia*
[c]*Department of Inorganic Chemistry, University of Chemistry and Technology Prague, Technická 5, 16628 Prague, Czech Republic*
[d]*School of Advanced Materials and Nanotechnology, Xidian University, Xi'an 710071, China*
[e]*2D Foundry Research Group, Instituto de Ciencia de Materiales de Madrid (ICMM-CSIC), 28049 Madrid, Spain*

Open Access Article. Published on 25 November 2025. Downloaded on 5/24/2026 7:43:23 PM.
This article is licensed under a Creative Commons Attribution-NonCommercial 3.0 Unported Licence.

This journal is © The Royal Society of Chemistry 2026

Open Access Article. Published on 25 November 2025. Downloaded on 5/24/2026 7:43:23 PM. This article is licensed under a Creative Commons Attribution-NonCommercial 3.0 Unported Licence.

the water inside before growth. The furnace was then heated up to 750–850 °C with a heating rate of 25–30 °C min^{-1} and kept at the growth temperature for 3–10 min. After growth, the furnace was cooled below 300 °C and then was opened for fast cooling to below 100 °C and the substrate was removed.

The flakes are transferred onto a flexible polycarbonate (PC) substrate with a thickness of 250 μm using a wet transfer method. A polydimethylsiloxane (PDMS) carrier substrate is first attached to the sample containing the WS_2 flakes. This assembly is then immersed in deionized water containing a small amount of ammonia, which facilitates the detachment of the PDMS layer along with the adhered flakes from the Si substrate. After detaching, the PDMS carrying the flakes is analyzed under the microscope to identify the flakes most suitable for transfer. The flakes are then mechanically transferred by gently pressing the PDMS against the PC substrate to ensure good contact, and by carefully peeling off the PDMS, leaving the WS_2 flakes securely attached to the PC substrate.[39]

To apply controlled uniaxial strain to the WS_2 flakes, a three-point bending setup adapted from ref. 40 and depicted in Fig. 1, right, was used. It consists of two identical manual linear micrometer Z stages, fixed onto a steel plate and supplemented with two homebuilt steel parts to attach the three cylinders that act as the pivots of the three-point-bending setup. The sample is placed in the central pivot, while the other pivots deflect the substrate from the sides, bending the sample and thus generating the uniaxial strain. This design ensures that the position of the sample remains nearly unchanged during the strain loading/unloading cycles. This eliminates the need for re-focusing and re-positioning the sample upon changing the strain in the optical measurements. We can achieve micrometric precision in controlling the deflection of the substrate, *i.e.* the displacement along the z-axis of the outer pivots. The applied strain ε is related to the distance D between the pivotal points, the deflection L, and the thickness t of the substrate by the following formula:

$$\varepsilon = \frac{6Lt}{D^2} \quad (1)$$

This formula has been validated experimentally in ref. 40.

Calculations of the ground-state electronic properties were carried out by using the GPAW open-source code[41] with a plane-wave cutoff energy of 600 eV. We use the van der Waals dispersion corrections vdW-DF[42] and vdW-DF2[43] for the exchange–correlation functional. The momentum grid for ground-state self-consistent calculations was set to $k = 24 \times 24 \times 1$, and we used Fermi–Dirac smearing with 0.01 eV broadening. Original unstrained structures were relaxed both in lateral and perpendicular directions, while for the strained slabs we only perform the interlayer relaxation. With vdW-DF, this gives $a = 3.186$ Å for both 0° and 60° stacking angles, and W–W interlayer distances of $d = 6.655$ Å and $d = 6.662$ Å for 60° and 0° stackings, respectively. When the relaxation is done with vdW-DF2, we get the same unit cell parameter a, while W–W distances for 60° and 0° stackings are $d = 6.578$ Å and $d = 6.583$ Å. For both stackings we obtain an S–S distance within the layer of 3.19 Å (3.23 Å) with vdW-DF (vdW-DF2). For a more accurate description of the quasiparticle spectra, we use both the HSE[44] and many-body G_0W_0 corrections.[45] In the latter case we used $k = 24 \times 24 \times 1$ points and 80 bands in order to converge the screened Coulomb propagator, and we used 80 eV energy cutoff for the G vectors. The quasiparticle G_0W_0 correction was applied only to the relevant top-most two valence bands, and to the lowest two conduction bands.

The calculations of the electron–phonon interaction were performed by means of density functional perturbation theory[46] and the Wannier interpolation[47] scheme as implemented in QuantumEspresso[48] and EPW[49] codes. Here we tried to use the same parameters as in GPAW calculations in order to match the electronic properties as obtained with the two codes. For the pseudopotentials we used the norm-conserving PBE functional from the PseudoDojo library,[50] and we also use vdW-DF dispersion correction. The lattice parameters were the same as in GPAW inputs. For the phonon calculations we used $k = 12 \times 12 \times 1$ and $q = 6 \times 6 \times 1$ grids. In EPW calculations we use 22 maximally localized Wannier functions with the initial projections of d orbitals on the W sites and p orbitals on the S atom sites. Calculations of the Fan-Migdal electron self-energy that accounts for the electron–phonon coupling within the band structures[51] are carried out on a $q = 120 \times 120 \times 1$ momentum grid.

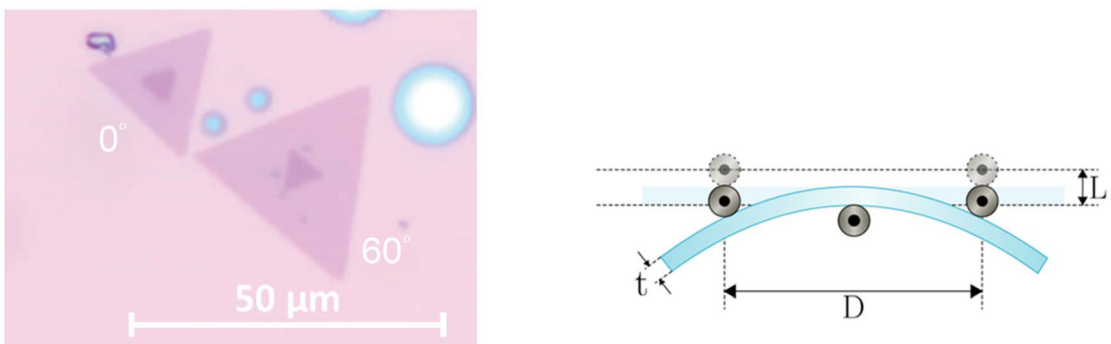

Fig. 1 Optical micrograph of as-grown bilayer flakes grown on SiO_2/Si before their transfer (left), and a scheme of the 3-point bending setup for strain investigation under an optical microscope (right).

Open Access Article. Published on 25 November 2025. Downloaded on 5/24/2026 7:43:23 PM.
This article is licensed under a Creative Commons Attribution-NonCommercial 3.0 Unported Licence.

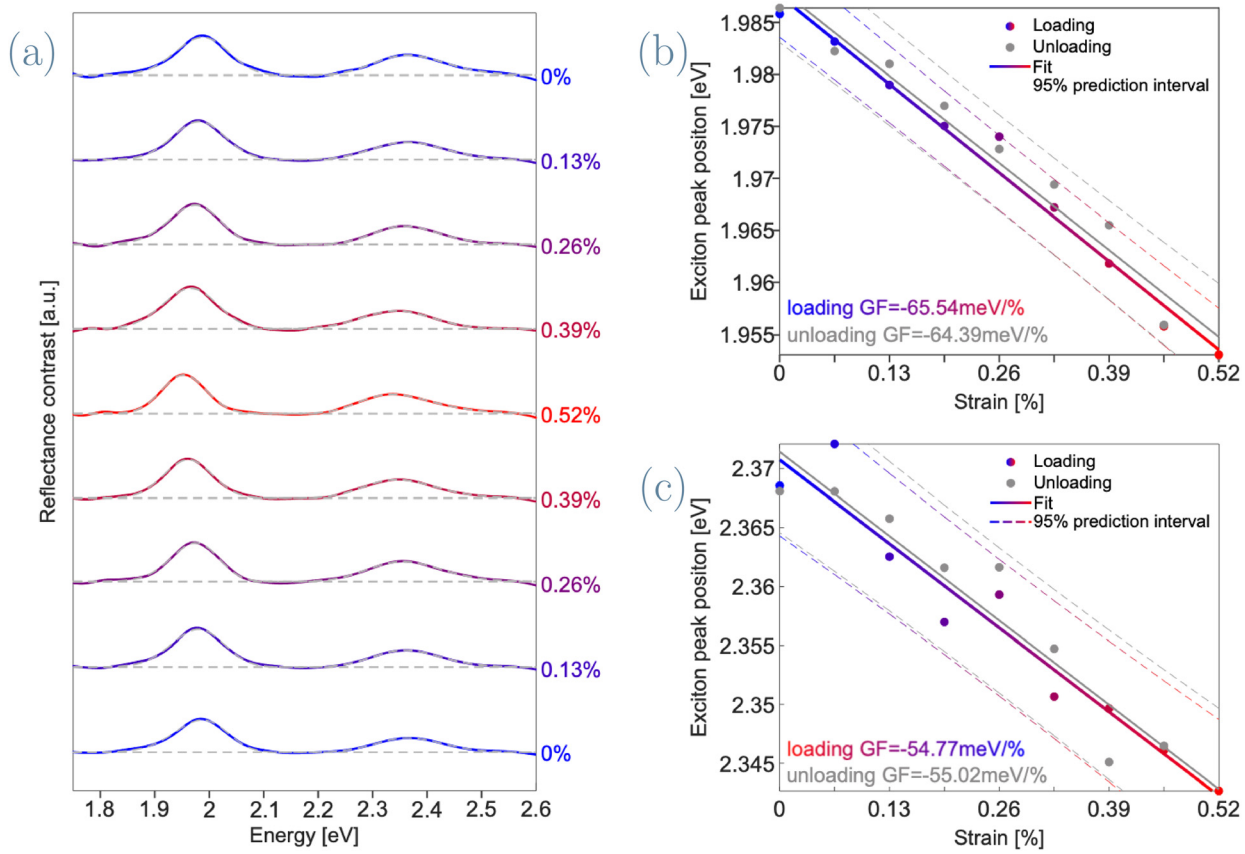

Fig. 2 (a) DR spectra of a 0° stacked WS_2 flake under strain from 0% to 0.52% and back to 0%. The curves are vertically shifted for clarity and drawn bottom to top in order of data acquisition. Determination of the strain GFs for the A exciton resonance (b) and the B exciton resonance (c).

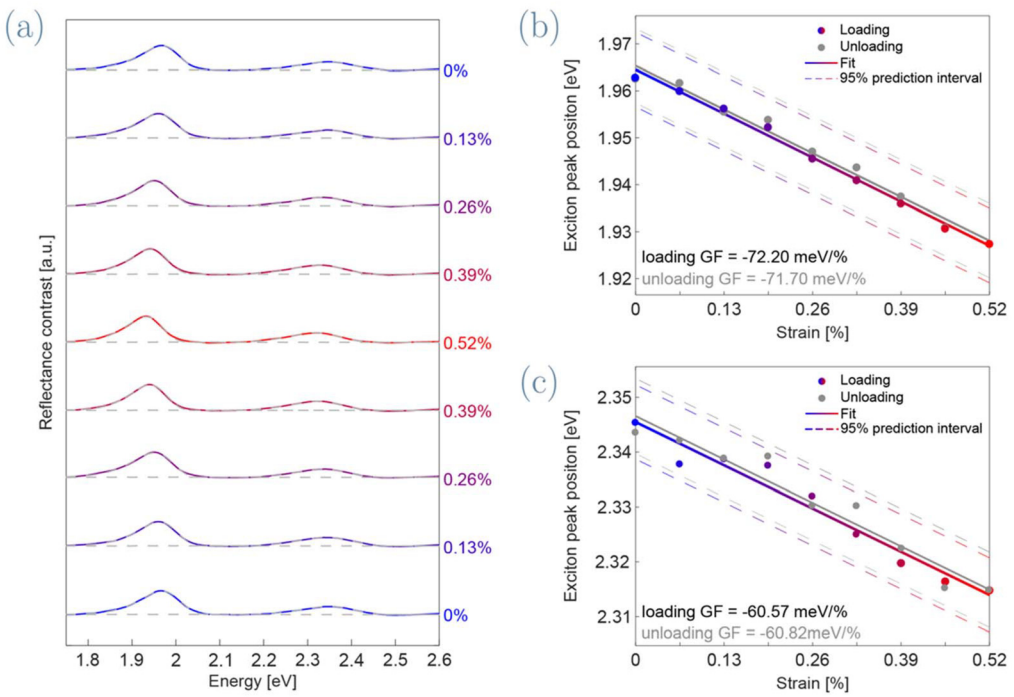

Fig. 3 (a) DR spectra of a 60° stacked WS_2 flake under strain from 0% to 0.52% and back to 0%. The curves are vertically shifted for clarity and drawn from bottom to top in order of data acquisition. Determination of the strain GFs for the A exciton resonance (b) and the B exciton resonance (c).

This journal is © The Royal Society of Chemistry 2026

Open Access Article. Published on 25 November 2025. Downloaded on 5/24/2026 7:43:23 PM.
This article is licensed under a Creative Commons Attribution-NonCommercial 3.0 Unported Licence.

Results and discussion

Bilayer flakes with 0° and 60° stacking angles were synthesized using chemical vapor deposition.[33,37,38] Representative optical micrographs of both stackings are shown in Fig. 1, left. The flakes are either hexagonal or triangular in shape, with the hexagonal ones typically having three long and three short edges, resembling triangles with truncated corners. Typical edge lengths of the (truncated) triangles are tens of μm. For 0° stacking, both top and bottom WS_2 layers appear as flakes with their (truncated) triangles oriented parallel to each other, while for 60° stacking they are rotated by 60°.[52–57]

For strain dependent DR spectroscopy, a total of twelve flakes of 0° and thirteen flakes of 60° stacking angle were transferred onto flexible PC substrates. The DR is measured by illuminating the sample on a spot approximately 1.5 μm in diameter with white light from a halogen lamp and collecting the reflected light. Strain is applied by bending the substrate in a loading (increasing strain) followed by an unloading sequence.[58] The DR spectra, shown in Fig. 2 and 3 for one example of each stacking angle, are dominated by the absorption of WS_2, showing the characteristic A and B exciton resonances.[59,60] To analyze the strain-dependent changes in the electronic structure, we fitted these spectra with a second-order polynomial to account for the scattering background and two skewed Gaussians to represent the main peaks broadened by electron–phonon coupling.[61,62] For the unstrained samples, we obtained the A and B resonances at 1.979 ± 0.002 eV and 2.357 ± 0.002 eV for 0° stacking and 1.986 ± 0.003 eV and 2.371 ± 0.006 eV for 60° stacking. In both cases, the A and B resonances shift linearly to the red with increasing strain and reproducibly return almost to their original spectral positions upon strain release with only minor hysteresis. The slopes of the linear fits in Fig. 2b, c and 3b,c yield the experimental strain GFs.

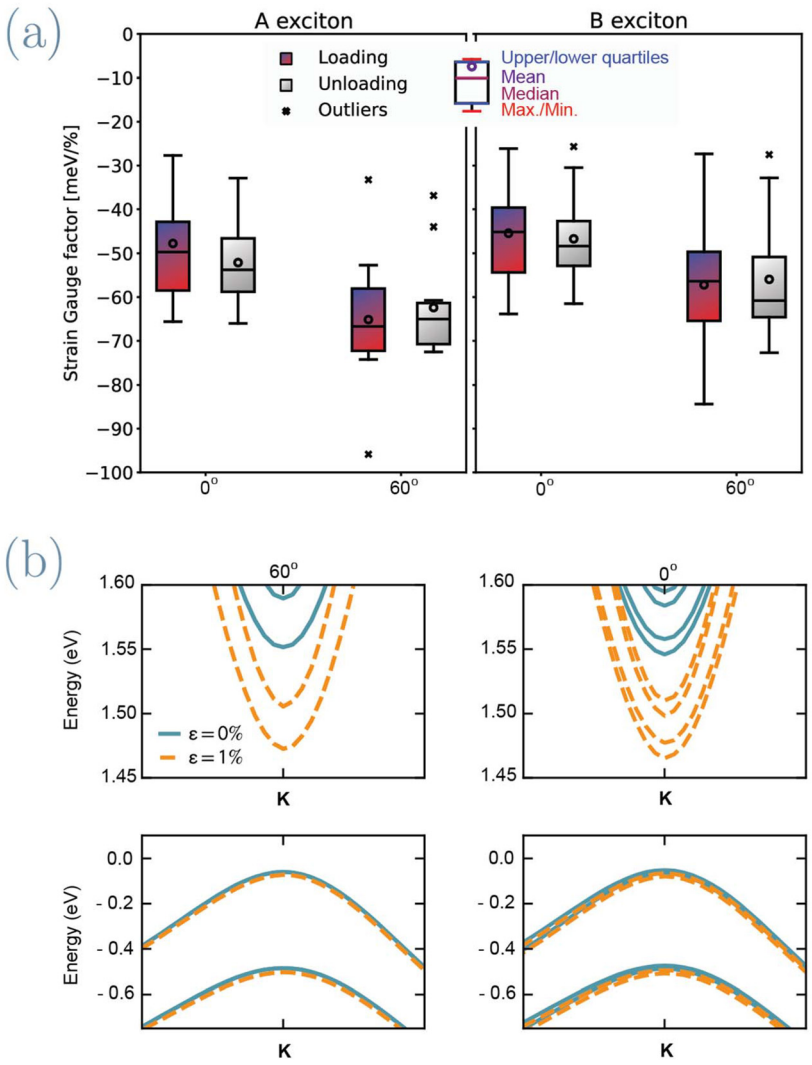

Fig. 4 (a) Statistical analysis of the strain GFs for excitons A and B in 0° and 60° stacking bilayers of WS_2 on various flakes. (b) The energy bands of bilayer WS_2 for 0° and 60° stacking angles calculated using density functional theory.

Open Access Article. Published on 25 November 2025. Downloaded on 5/24/2026 7:43:23 PM.
This article is licensed under a Creative Commons Attribution-NonCommercial 3.0 Unported Licence.

The statistical analysis of the 12 0°-stacked and the 13 60°-stacked flakes shown in Fig. 4a and Table 1 yields strain GFs whose absolute values are about 10% higher for the A than the B resonance, and 25% higher for 60° than for 0° stacking. The calculated band structures in Fig. 4b show that at the *K* point, where the electronic transitions associated with the A and B resonances take place, the conduction bands shift to lower energy upon strain application, while the valence bands remain almost unaffected, resulting in red-shifted optical transitions with GFs in good agreement with the experimental values (see Table 1). According to our theoretical analysis, a small difference between the strain GFs of the A and B excitons could arise from the modification of spin–orbit coupling with strain. For instance, in the case of 0° stacking the spin–orbit-coupling splitting between the valence bands is 422 meV, which is then modified to 428 meV upon 1% strain. A similar effect is observed for 60° stacking, where the splitting increases from 425 meV to 430 meV with 1% strain. The increase of the spin–orbit splitting counteracts the strain-induced decrease of the band gap and therefore results in a lower absolute strain GF for the B exciton compared to the A exciton.

Table 1 Experimental and calculated strain GFs for A and B excitons in WS_2 for 0° and 60° stacking angle

	A_0	A_{60}	B_0	B_{60}
Exp. mean (meV per %)	−50 ± 2	−64 ± 3	−46 ± 2	−57 ± 4
Exp. median (meV per %)	−51	−66	−47	−59
Calculated (meV per %)	−73	−76	−61	−66

The theoretical results presented in Table 1 are obtained with G_0W_0 as well as with the inclusion of electron–phonon renormalization to the electron energies, when the structure is relaxed with vdW-DF2 functional. In that case, the GF of A exciton for 60° is around 4% higher than for 0° stacking. With only G_0W_0 one obtains GFs of −80 meV per % and −81.3 meV per % for 0° and 60° stackings, respectively. Very similar results are obtained with HSE functional [GF(0°) = −81.3 meV per % and GF(60°) = −82.7 meV per %], as well as with the HSE functional when the structure is relaxed with vdW-DF2 [GF(0°) = −79.5 meV per % and GF(60°) = −80.4 meV per %]. Besides that we note that the results obtained without HSE or G_0W_0 provide the trend that opposes the experimentally observed GFs. Namely, in that case we obtain GF(0°) = −76.8 meV per % and GF(60°) = −67 meV per % for structures relaxed with both vdW-DF and vdW-DF2. With this one concludes that theory provides very similar results for GFs, but with slightly higher value for the 60° stacking, in agreement with the experimental observation, especially when both the non-local electron–electron (beyond semi-local PBE and vdW corrections) and electron–phonon corrections are included. This highlights the need to include non-local electron–electron and electron–phonon interaction to accurately model the stacking dependence of the strain GFs.

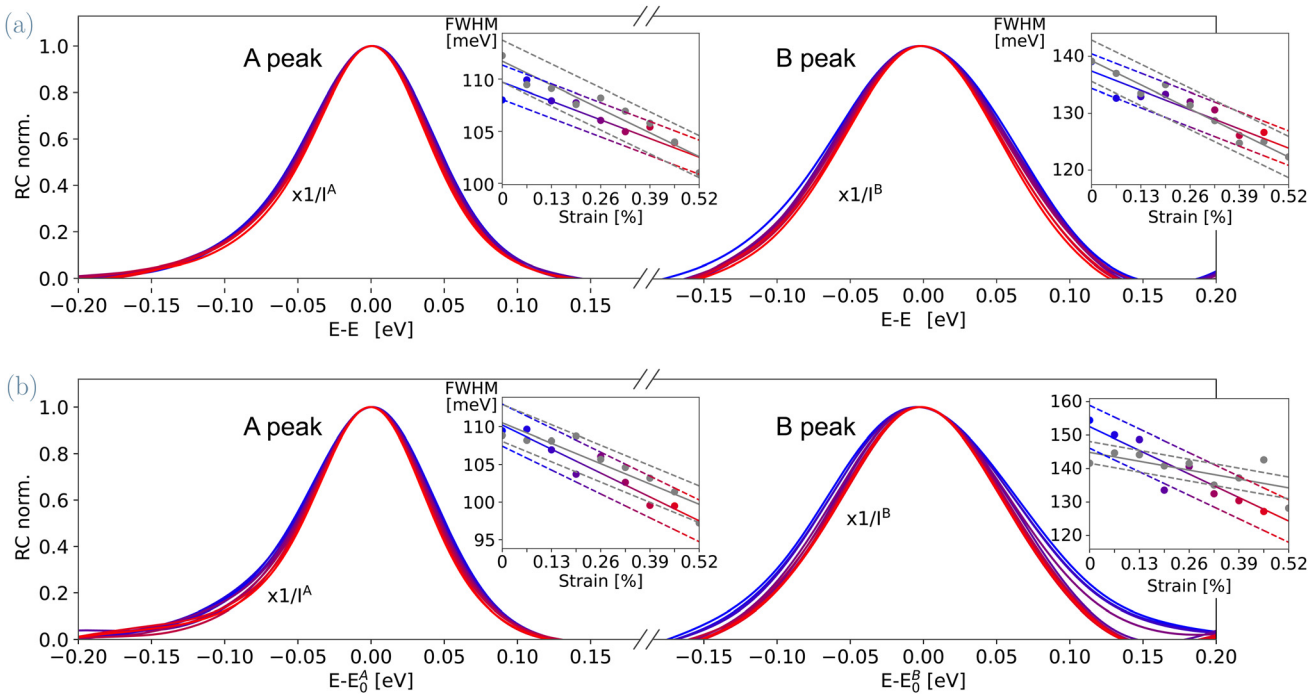

Fig. 5 FWHM variation in the reflectance contrast spectra of 2L-WS_2 at different applied strains for one flake each in 0° (a) and 60° (b) stacking angle. On the left side, the spectra of the A peak, normalized with respect to its intensity and centered at the A peak center are presented, highlighting the variation in FWHM as a function of strain. On the right side, the spectra of the B exciton peak, normalized and centered, are shown. Inset graphs show the strain-dependent FWHMs as a function of the applied strain.

This journal is © The Royal Society of Chemistry 2026

Open Access Article. Published on 25 November 2025. Downloaded on 5/24/2026 7:43:23 PM.
This article is licensed under a Creative Commons Attribution-NonCommercial 3.0 Unported Licence.

We additionally note that the Q valley (shown later) is only slightly affected by the strain, so that the energy difference between the valence K valley and conduction Q valley is almost unchanged.

We will now examine how strain affects the A and B peak widths, which are determined by the electron–phonon coupling. Examples for the strain-dependent full width at half maximum (FWHM) values are given in Fig. 5 for the A and B peaks in both stacking angles. For the unstrained samples, the FWHMs statistically averaged over all flakes are 106 ± 1 meV and 144 ± 1 meV for A and B in 0° stacking and 122 ± 4 meV and 146 ± 3 meV for 60° stacking. Upon strain application, the A and B peaks in both stackings become progressively higher and narrower, without a significant change of their area. Hence, strain reduces the widths of the excitonic resonances without appreciably changing their oscillator strength. Again, the effect is stronger for 60° stacking, though to a lesser extent than for the resonance energies.

In Fig. 6 we show the results for the calculations of the electron–phonon scattering and its impact on the electron and hole state broadening when uniaxial strain is applied on 2L WS_2 with 60° stacking angle. Panel (a) shows the modification of the electron–phonon-induced scattering rate of valence and conduction band states when the system is strained by 1%. The biggest change in broadening occurs for the conduction band valley around the *K* point, where the scattering rate is reduced by ~20 meV. The broadening of the valence band states at the *K* point is increased by less than that; hence the net effect is that the broadening of the electron–hole excitations is decreased for the excitation energies close to the band gap. In the simplest approach, the combined broadening of electron and hole pairs is a solid approximation for the scattering rate of electron–hole bound states, *i.e.*, excitons,[63] so the presented results serve as a qualitative explanation for the behavior of the exciton FWHM as a function of strain as obtained in Fig. 5. In fact, we show that the strain-induced decrease of the FWHM of A and B excitons in 2L WS_2 could be explained through the reduced electron–phonon scattering rate of conduction electrons in the K valley, which in turn comes from the strain-induced modified scattering phase space between Q

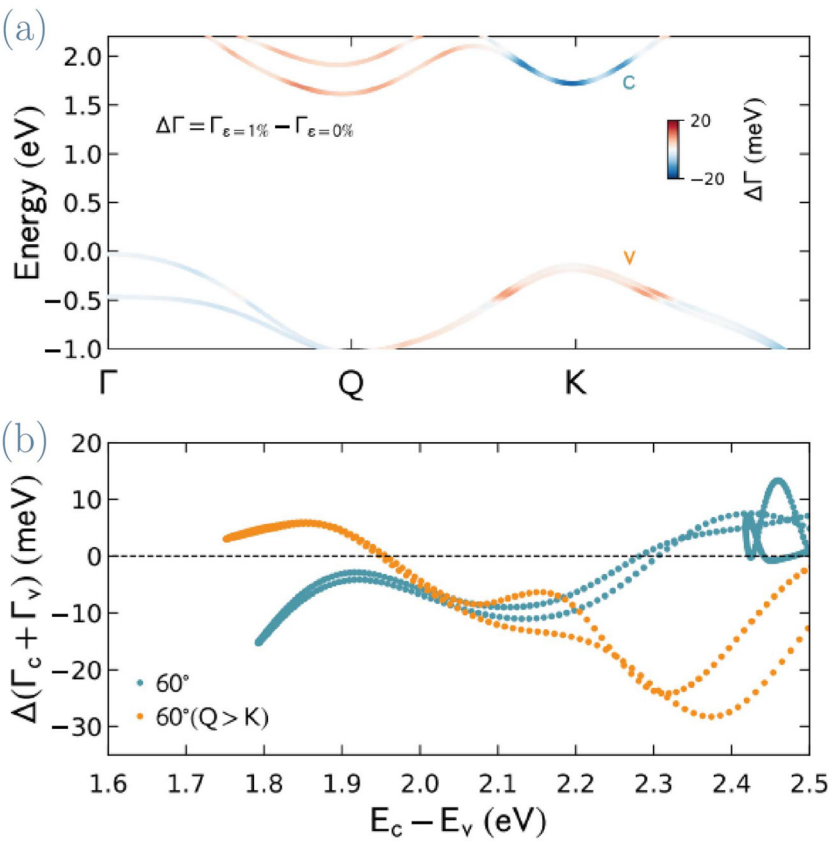

Fig. 6 The impact of strain on electron–phonon-related broadening of electron–hole excitations in 2L WS_2 with 60° stacking angle. (a) Band structure of valence and conduction states where the color depicts the change of the electron state broadening due to applied uniaxial strain of 1%. The conduction (valence) states around the K valley show decrease (increase) of the electron–phonon-related broadening. (b) The total change of the electron–hole scattering rate due to strain as a function of electron–hole excitation energy. The blue dots show the results for the 60° stacking angle, while the orange dots are for the same stacking configuration but when the S–S distance is altered so that the energy of the Q valley is lifted above the K valley. The results show that the broadening of the electron–hole excitations (such as excitons) would decrease with applied strain if the energy of the K valley were above the Q valley.

Open Access Article. Published on 25 November 2025. Downloaded on 5/24/2026 7:43:23 PM. This article is licensed under a Creative Commons Attribution-NonCommercial 3.0 Unported Licence.

and K valleys. In particular, the applied strain shifts the Q valley to higher energies,[64] which reduces the scattering phase space for the K valley. This effect is reversed when the original unstrained structure of 2L WS_2 is adjusted in such a way that the energy of the Q valley is above the K valley (orange dots). Therefore, the negative trend of FWHMs in 2L WS_2 indicates that these materials are indirect gap semiconductors, or at the very edge of direct-to-indirect band-gap transition.[34,35]

Both the 0° and 60° stacking angles have rather similar small interlayer distances (0.662 and 0.655 nm, respectively), and consequently similar strong interlayer coupling. For stacking angles between 0 and 60°, larger interlayer distances and consequently weaker coupling is found.[65] An increase in interlayer spacing raises the energy of indirect ($\Lambda \rightarrow \Gamma$ and $K \rightarrow \Gamma$) electronic transitions, while the direct $K \rightarrow K$ transition energy remains nearly unchanged.[66] This trend leads to an indirect-to-direct gap crossover at large interlayer spacing. For 0° and 60° stacking, the bilayers have an indirect band gap, as seen in Fig. 6a. Despite the calculated high sensitivity of the valence band maximum at the Γ point, for the applied strain values up to 0.52%, no direct-to-indirect band gap crossover is expected. Such crossovers usually appear as kinks in either the strain-dependent peak positions or widths.[13,25] The absence of such kinks in our experimental data confirms that the band gap remains indirect over the observed strain range.

Conclusion

Our joint experimental and computational investigation highlights the stacking dependent linear strain GFs of the excitonic resonance energies and the electron–phonon coupling strength of bilayer WS_2. Both examined stacking angles have low interlayer distance and strong interlayer coupling. Even stronger effects can be expected if intermediate stacking angles are included, where a much larger variation of the interlayer coupling leads to a quasi-direct bandgap behavior and the appearance of an interlayer exciton. Our work is a first step towards synergistic harnessing of both strain and twist angles as control parameters for the functionality of two-dimensional semiconductors. For example, the twist angle could be used to calibrate the sensitivity of a strain sensor or to adjust the signal weight in neuromorphic straintronic devices.[67]

Author contributions

I. L.-G., V. J. and B. R. carried out the strain-dependent optical experiments.

Q. L. fabricated the samples.

D. N. performed the calculations.

I. L.-G. and V. J. analyzed and visualized the data.

N. V., A. C.-G., C. G. and X. Y. provided funding and supervised the work.

C. G., D. N., I. L.-G. and V. J. wrote the paper with input from all authors.

Conflicts of interest

There are no conflicts to declare.

Abbreviations

TMDC	Transition metal dichalcogenide
DR	Differential reflectance
GF	Gauge factor
PC	Polycarbonate
PDMS	Polydimethylsiloxane
FWHM	Full width at half maximum

Data availability

Raw data is available on https://drive.google.com/drive/folders/1vEs91D4aqiCYMXz03WhyRq2MQGDPxY-o?usp=share_link.

Acknowledgements

This work received funding from the European Union's Horizon 2020 research and innovation program under grant agreement 956813 (2Exciting). D. N. and N. V. acknowledge support by the Centre of Excellence for Advanced Materials and Sensing Devices (Grant No. KK.01.1.1.01.0001) and Centre for Advanced Laser Techniques (Grant No. KK.01.1.1.05.0001) co-financed by the Croatian Government and the European Union through the European Regional Development Fund – Competitiveness and Cohesion Operational Program. A.C-G. acknowledges support from Grants PDC2023-145920-I00 and PID2023-151946OB-I00, funded by MICIU/AEI/10.13039/501100011033 and, respectively, by the European Union NextGenerationEU/PRTR (PDC2023-145920-I00) and by ERDF/EU (PID2023-151946OB-I00). A.C-G. also acknowledges funding from the European Research Council (ERC) through the ERC-PoC 2024 StEnSo project (grant agreement 101185235). ICMM-CSIC authors acknowledges support from the Severo Ochoa Centres of Excellence program through Grant CEX2024-001445-S, funded by MICIU/AEI/10.13039/501100011033. This work was supported by the Open Fund of State Key Laboratory of Infrared Physics (Grant No. SITP-NLIST-ZD-2024-01). I. L.-G., V. J. and C. G. acknowledge support by the PRIN 2020 project Conquest funded by the Italian Ministry of University and Research (Prot. 2020JZ5N9M).

References

1 Z. Yin, H. Li, H. Li, L. Jiang, Y. Shi, Y. Sun, G. Lu, Q. Zhang, X. Chen and H. Zhang, Single-Layer MoS_2 Phototransistors, *ACS Nano*, 2012, **6**, 74–80, DOI: 10.1021/nn2024557.

 This journal is © The Royal Society of Chemistry 2026

Open Access Article. Published on 25 November 2025. Downloaded on 5/24/2026 7:43:23 PM. This article is licensed under a Creative Commons Attribution-NonCommercial 3.0 Unported Licence.

2 M. Fontana, T. Deppe, A. K. Boyd, M. Rinzan, A. Y. Liu, M. Paranjape and P. Barbara, Electron-Hole Transport and Photovoltaic Effect in Gated MoS_2 Schottky Junctions, *Sci. Rep.*, 2013, **3**, 1–6, DOI: 10.1038/srep01634.

3 H. Zhang, S. B. Lu, J. Zheng, J. Du, S. C. Wen, D. Y. Tang and K. P. Loh, Molybdenum Disulfide (MoS_2) as a Broadband Saturable Absorber for Ultra-Fast Photonics, *Opt. Express*, 2014, **22**, 7249, DOI: 10.1364/OE.22.007249.

4 Y. Ye, Z. J. Wong, X. Lu, X. Ni, H. Zhu, X. Chen, Y. Wang and X. Zhang, Monolayer Excitonic Laser, *Nat. Photonics*, 2015, **9**, 733–737, DOI: 10.1038/nphoton.2015.197.

5 R. Peng, L. Liang, Z. D. Hood, A. Boulesbaa, A. Puretzky, A. V. Ievlev, J. Come, O. S. Ovchinnikova, H. Wang, C. Ma, M. Chi, B. G. Sumpter and Z. Wu, In-Plane Heterojunctions Enable Multiphasic Two-Dimensional (2D) MoS_2 Nanosheets As Efficient Photocatalysts for Hydrogen Evolution from Water Reduction, *ACS Catal.*, 2016, **6**, 6723–6729, DOI: 10.1021/acscatal.6b02076.

6 D. Vella, D. Ovchinnikov, N. Martino, V. Vega-Mayoral, D. Dumcenco, Y.-C. Kung, M.-R. Antognazza, A. Kis, G. Lanzani, D. Mihailovic and C. Gadermaier, Unconventional Electroabsorption in Monolayer MoS_2, *2D Mater.*, 2017, **4**, 021005, DOI: 10.1088/2053-1583/aa5784.

7 C. Trovatello, A. Marini, X. Xu, C. Lee, F. Liu, N. Curreli, C. Manzoni, S. Dal Conte, K. Yao, A. Ciattoni, J. Hone, X. Zhu, P. J. Schuck and G. Cerullo, Optical parametric amplification by monolayer transition metal dichalcogenides, *Nat. Photonics*, 2021, **15**, 6–10, DOI: 10.1038/s41566-020-00728-0.

8 R. Roldàn, A. Castellanos-Gomez, E. Cappelluti and F. Guinea, *J. Phys.: Condens. Matter*, 2015, **27**, 313201, DOI: 10.1088/0953-8984/27/31/313201.

9 J. Kern, I. Niehues, P. Tonndorf, R. Schmidt, D. Wigger, R. Schneider, T. Stiehm, S. Michaelis de Vasconcellos, D. E. Reiter, T. Kuhn and R. Bratschitsch, Nanoscale Positioning of Single-Photon Emitters in Atomically Thin WSe_2, *Adv. Mater.*, 2016, **28**, 7101–7105, DOI: 10.1002/adma.201600560.

10 S. B. Desai, G. Seol, J. S. Kang, H. Fang, C. Battaglia, R. Kapadia, J. W. Ager, J. Guo and A. Javey, Strain-Induced Indirect to Direct Bandgap Transition in Multilayer WSe_2, *Nano Lett.*, 2014, **14**, 4592–4597, DOI: 10.1021/nl501638a.

11 G. Plechinger, A. Castellanos-Gomez, M. Buscema, H. S. J. Van Der Zant, G. A. Steele, A. Kuc, T. Heine, C. Schüller and T. Korn, Control of biaxial strain in single-layer molybdenite using local thermal expansion of the substrate, *2D Mater.*, 2015, **2**, 015006, DOI: 10.1088/2053-1583/2/1/015006.

12 C. R. Zhu, G. Wang, B. L. Liu, X. Marie, X. F. Qiao, X. Zhang, X. X. Wu, H. Fan, P. H. Tan, T. Amand and B. Urbaszek, Strain tuning of optical emission energy and polarization in monolayer and bilayer MoS_2, *Phys. Rev. B: Condens. Matter Mater. Phys.*, 2013, **88**, 121301(R), DOI: 10.1103/PhysRevB.88.121301.

13 H. J. Conley, B. Wang, J. I. Ziegler, R. F. Haglund Jr., S. T. Pantelides and K. I. Bolotin, Bandgap Engineering of Strained Monolayer and Bilayer MoS_2, *Nano Lett.*, 2013, **13**, 3626–3630, DOI: 10.1021/nl4014748.

14 A. Castellanos-Gomez, R. Roldán, E. Cappelluti, M. Buscema, F. Guinea, H. S. J. van der Zant and G. A. Steele, Local Strain Engineering in Atomically Thin MoS_2, *Nano Lett.*, 2013, **13**, 5361–5366, DOI: 10.1021/nl402875m.

15 B. Amin, T. P. Kaloni and U. Schwingenschlögl, Strain engineering of WS_2, WSe_2, and WTe_2, *RSC Adv.*, 2014, **4**, 34561, DOI: 10.1039/C4RA06378C.

16 Y. Wang, C. Cong, W. Yang, J. Shang, N. Peimyoo, Y. Chen, J. Kang, J. Wang, W. Huang and T. Yu, Strain-induced direct–indirect bandgap transition and phonon modulation in monolayer WS_2, *Nano Res.*, 2015, **8**, 2562–2572, DOI: 10.1007/s12274-015-0762-6.

17 H. Shi, H. Pan, Y.-W. Zhang and B. I. Yakobson, Quasiparticle band structures and optical properties of strained monolayer MoS_2 and WS_2, *Phys. Rev. B:Condens. Matter Mater. Phys.*, 2013, **87**, 155304, DOI: 10.1103/PhysRevB.87.155304.

18 R. Schmidt, I. Niehues, R. Schneider, M. Drüppel, T. Deilmann, M. Rohlfing, S. Michaelis de Vasconcellos, A. Castellanos-Gomez and R. Bratschitsch, Reversible uniaxial strain tuning in atomically thin WSe_2, *2D Mater.*, 2016, **3**, 021011, DOI: 10.1088/2053-1583/3/2/021011.

19 J. O. Island, A. Kuc, E. H. Diependaal, R. Bratschitsch, H. S. J. van der Zandt, T. Heine and A. Castellanos-Gomez, Precise and reversible band gap tuning in single-layer $MoSe_2$ by uniaxial strain, *Nanoscale*, 2016, **8**, 2589, DOI: 10.1039/c5nr08219f.

20 W. Hu, Y. Wang, K. He, X. He, Y. Bai, C. Liu, N. Zhou, H. Wang, P. Li, X. Ma and Y. Xie, Straining of atomically thin WSe_2 crystals: Suppressing slippage by thermal annealing, *J. Appl. Phys.*, 2022, **132**, 085105, DOI: 10.1063/5.0096190.

21 K. He, C. Poole, K. F. Mak and J. Shan, Experimental Demonstration of Continuous Electronic Structure Tuning via Strain in Atomically Thin MoS_2, *Nano Lett.*, 2013, **13**, 2931–2936, DOI: 10.1021/nl4013166.

22 I. Niehues, A. Blob, T. Stiehm, R. Schmidt, V. Jadriško, B. Radatović, D. Čapeta, M. Kralj, S. Michaelis de Vasconcellos and R. Bratschitsch, Strain transfer across grain boundaries in MoS_2 monolayers grown by chemical vapor deposition, *2D Mater.*, 2018, **5**, 031003, DOI: 10.1088/2053-1583/aaba9a.

23 P. V. Kolesnichenko, Q. Zhang, T. Yun, C. Zheng, M. S. Fuhrer and J. A. Davis, Disentangling the effects of doping, strain and disorder in monolayer WS_2 by optical spectroscopy, *2D Mater.*, 2020, **7**, 025008, DOI: 10.1088/2053-1583/ab626a.

24 I. Niehues, R. Schmidt, M. Drüppel, P. Marauhn, D. Christiansen, M. Selig, G. Berghäuser, D. Wigger, R. Schneider, L. Braasch, R. Koch, A. Castellanos-Gomez, T. Kuhn, A. Knorr, E. Malic, M. Rohlfing, S. Michaelis de Vasconcellos and R. Bratschitsch, Strain Control of Exciton–Phonon Coupling in Atomically Thin

Open Access Article. Published on 25 November 2025. Downloaded on 5/24/2026 7:43:23 PM. This article is licensed under a Creative Commons Attribution-NonCommercial 3.0 Unported Licence.

Semiconductors, *Nano Lett.*, 2018, **18**, 1751–1757, DOI: 10.1021/acs.nanolett.7b04868.

25 O. B. Aslan, M. Deng, M. L. Brongersma and T. F. Heinz, Strained bilayer WSe_2 with reduced exciton-phonon coupling, *Phys. Rev. B*, 2020, **101**, 115305, DOI: 10.1103/PhysRevB.101.115305.

26 W. S. Yun, S. W. Han, S. C. Hong, I. G. Kim and J. D. Lee, hickness and strain effects on electronic structures of transition metal dichalcogenides: 2H-*MX*2 semiconductors (*M* = Mo, W; *X* = S, Se, Te), *Phys. Rev. B:Condens. Matter Mater. Phys.*, 2012, **85**, 033305, DOI: 10.1103/PhysRevB.85.033305.

27 J. Feng, X. Qian, C.-W. Huang and J. Li, Strain-engineered artificial atom as a broad-spectrum solar energy funnel, *Nat. Photonics*, 2012, **6**, 866–872, DOI: 10.1038/nphoton.2012.285.

28 C. Rice, R. J. Young, R. Zan, U. Bangert, D. Wolverson, T. Georgiou, R. Jalil and K. S. Novoselov, Raman-scattering measurements and first-principles calculations of strain-induced phonon shifts in monolayer MoS_2, *Phys. Rev. B: Condens. Matter Mater. Phys.*, 2013, **87**, 081307(R), DOI: 10.1103/PhysRevB.87.081307.

29 S. Yu, H. D. Xiong, K. Eshun, H. Yuan and Q. L. Li, Phase transition, effective mass and carrier mobility of MoS_2 monolayer under tensile strain, *Appl. Surf. Sci.*, 2015, **325**, 27–32, DOI: 10.1016/j.apsusc.2014.11.079.

30 Y. Chen, D. Lu, L. Kong, Q. Tao, L. Ma, L. Liu, Z. Lu, Z. Li, R. Wu, X. Duan, L. Liao and Y. Liu, Mobility Enhancement of Strained MoS_2 Transistor on Flat Substrate, *ACS Nano*, 2023, **17**, 14954–14962, DOI: 10.1021/acsnano.3c03626.

31 A. Kayal, S. Dey, G. Harikrishnan, R. Nadarajan, S. Chattopadhyay and J. Mitra, Mobility Enhancement in CVD-Grown Monolayer MoS_2 Via Patterned Substrate-Induced Nonuniform Straining, *Nano Lett.*, 2023, **23**, 6629–6636, DOI: 10.1021/acs.nanolett.3c01774.

32 S. Yu, H. Zhu, K. Eshun, C. Shi, M. Zeng and Q. L. Li, Strain-engineering the anisotropic electrical conductance in ReS_2 monolayer, *Appl. Phys. Lett.*, 2016, **108**, 191901, DOI: 10.1063/1.4947195.

33 H. Yang, R. Hu, H. Wu, X. He, Y. Zhou, Y. Xue, K. He, W. Hu, H. Chen, M. Gong, X. Zhang, P.-H. Tan, E. R. Hernández and Y. Xie, Identification and Structural Characterization of Twisted Atomically Thin Bilayer Materials by Deep Learning, *Nano Lett.*, 2024, **24**, 2789, DOI: 10.1021/acs.nanolett.3c04815.

34 Y. Yu, C.-D. Dong, R. Binder, S. Schumacher and C.-Z. Ning, Strain-Induced Indirect-to-Direct Bandgap Transition, Photoluminescence Enhancement, and Linewidth Reduction in Bilayer $MoTe_2$, *ACS Nano*, 2023, **17**, 4230–4238, DOI: 10.1021/acsnano.2c01665.

35 Z. Khatibi, M. Feierabend, M. Selig, S. Brem, C. Linderälv, P. Erhart and E. Malic, Impact of strain on the excitonic linewidth in transition metal dichalcogenides, *2D Mater.*, 2018, **6**, 015015, DOI: 10.1088/2053-1583/aae953.

36 I. Niehues, P. Marauhn, T. Deilmann, D. Wigger, R. Schmidt, A. Arora, S. Michaelis de Vasconcellos, M. Rohlfing and R. Bratschitsch, Strain tuning of the Stokes shift in atomically thin Semiconductors, *Nanoscale*, 2020, **12**, 20786–20796, DOI: 10.1039/D0NR04557H.

37 Y. Xie, Z. Wang, Y. Zhan, P. Zhang, R. Wu, T. Jiang, S. Wu, H. Wang, Y. Zhao, T. Nan and X. Ma, Controllable growth of monolayer MoS_2 by chemical vapor deposition via close MoO_2 precursor for electrical and optical applications, *Nanotechnology*, 2017, **28**, 084001, DOI: 10.1088/1361-6528/aa5439.

38 Z. Wang, Y. Xie, H. Wang, R. Wu, T. Nan, Y. Zhan, J. Sun, T. Jiang, Y. Zhao, Y. Lei, M. Yang, W. Wang, Q. Zhu, X. Ma and Y. Hao, NaCl-assisted one-step growth of MoS_2–WS_2 in-plane heterostructures, *Nanotechnology*, 2017, **28**, 325602, DOI: 10.1088/1361-6528/aa6f01.

39 A. Castellanos-Gomez, M. Buscema, R. Molenaar, V. Singh, L. Janssen, H. S. J. van der Zant and G. A. Steele, Deterministic transfer of two-dimensional materialsby all-dry viscoelastic stamping, *2D Mater.*, 2014, **1**, 011002, DOI: 10.48550/arXiv.1311.4829.

40 F. Carrascoso, H. Li, R. Frisenda and A. Castellanos-Gomez, Strain engineering in single-, bi- and tri-layer MoS_2, $MoSe_2$, WS_2 and WSe_2, *Nano Res.*, 2021, **14**, 1698–1703, DOI: 10.1007/s12274-020-2918-2.

41 J. J. Mortensen, A. H. Larsen, M. Kuisma, A. V. Ivanov, A. Taghizadeh, A. Peterson, A. Haldar, A. O. Dohn, C. Schäfer, E.Ö Jónsson, E. D. Hermes, F. A. Nilsson, G. Kastlunger, G. Levi, H. Jónsson, H. Häkkinen, J. Fojt, J. Kangsabanik, J. Sødequist, J. Lehtomäki, *et al.*, GPAW: An open Python package for electronic structure calculations, *J. Chem. Phys.*, 2024, **160**, 092503, DOI: 10.1063/5.0182685.

42 M. Dion, H. Rydberg, E. Schroder, D. C. Langreth and B. I. Lundqvist, van der Waals Density Functional for General Geometries, *Phys. Rev. Lett.*, 2004, **92**, 246401, DOI: 10.1103/PhysRevLett.92.246401.

43 K. Lee, E. D. Murray, L. Kong, B. I. Lundqvist and D. C. Langreth, Higher-accuracy van der Waals density functional, *Phys. Rev. B:Condens. Matter Mater. Phys.*, 2010, **92**, 081101(R), DOI: 10.1103/PhysRevB.82.081101.

44 J. Heyd, G. E. Scuseria and M. Enzerhof, Hybrid functionals based on a screened Coulomb potential, *J. Chem. Phys.*, 2003, **119**, 8207–8215, DOI: 10.1063/1.1564060.

45 F. Huser, T. Olsen and K. S. Thygesen, Quasiparticle GW calculations for solids, molecules, and two-dimensional materials, *Phys. Rev. B:Condens. Matter Mater. Phys.*, 2013, **87**, 235132, DOI: 10.1103/PhysRevB.87.235132.

46 S. Baroni, S. de Gironcoli, A. Dal Corso and P. Giannozzi, Phonons and related crystal properties from density-functional perturbation theory, *Rev. Mod. Phys.*, 2001, **73**, 715, DOI: 10.1103/RevModPhys.73.515.

47 N. Marzari, A. A. Mostofi, J. R. Yates, I. Souza and D. Vanderbilt, Maximally localized Wannier functions: Theory and applications, *Rev. Mod. Phys.*, 2012, **84**, 1419, DOI: 10.1103/RevModPhys.84.1419.

48 P. Giannozzi, O. Andreussi, T. Brumme, O. Bunau, M. Buongiorno Nardelli, M. Calandra, R. Car, C. Cavazzoni, D. Ceresoli, M. Cococcioni, N. Colonna, I. Carnimeo, A. Dal Corso, S. de Gironcoli, P. Delugas, R. A. DiStasio Jr,

 This journal is © The Royal Society of Chemistry 2026

Open Access Article. Published on 25 November 2025. Downloaded on 5/24/2026 7:43:23 PM. This article is licensed under a Creative Commons Attribution-NonCommercial 3.0 Unported Licence.

A. Ferretti, A. Floris, G. Fratesi, G. Fugallo, *et al.* Advanced capabilities for materials modelling with Quantum ESPRESSO, *J. Phys.: Condens. Matter.*, 2017, **29**, 465901, DOI: 10.1088/1361-648X/aa8f79.

49 H. Lee, S. Poncé, K. Bushick, S. Hajinazar, J. Lafuente-Bartolome, J. Leveillee, C. Lian, J.-M. Lihm, F. Macheda, H. Mori, H. Paudyal, W. H. Sio, S. Tiwari, M. Zacharias, X. Zhang, N. Bonini, E. Kioupakis, E. R. Margine and F. Giustino, Electron-phonon physics from first principles using the EPW code, *Npj Comput. Mater.*, 2023, **9**, 156, DOI: 10.1038/s41524-023-01107-3.

50 M. J. van Setten, M. Giantomassi, E. Bousquet, M. J. Verstraete, D. R. Hamann, X. Gonze and G.-M. Rignanese, The PseudoDojo: Training and grading a 85 element optimized norm-conserving pseudopotential table, *Comp. Phys. Commun.*, 2018, **226**, 39–54, DOI: 10.1016/j.cpc.2018.01.012.

51 F. Giustino, Electron-phonon interactions from first principles, *Rev. Mod. Phys.*, 2017, **89**, 015003, DOI: 10.1103/RevModPhys.89.015003.

52 J. He, K. Hummer and C. Franchini, Stacking effects on the electronic and optical properties of bilayer transition metal dichalcogenides MoS_2, $MoSe_2$, WS_2, and WSe_2, *Phys. Rev. B: Condens. Matter Mater. Phys.*, 2014, **89**, 075409, DOI: 10.1103/PhysRevB.89.075409.

53 S. Yang, J. Kang, Q. Yue and K. Yao, Spectroscopic Signatures of AA' and AB Stacking of Chemical Vapor Deposited Bilayer MoS_2, *J. Phys. Chem. C*, 2014, **118**, 9203–9208.

54 M. Xia, B. Li, K. Yin, G. Capellini, G. Niu, Y. Gong, W. Zhou, P. M. Ajayan and Y.-H. Xie, Spectroscopic Signatures of AA' and AB Stacking of Chemical Vapor Deposited Bilayer MoS_2, *ACS Nano*, 2015, **9**, 12246–12254.

55 J. Yan, *et al.*, Stacking-Dependent Interlayer Coupling in Trilayer MoS_2 with Broken Inversion Symmetry, *Nano Lett.*, 2015, **15**, 8155–8161.

56 V. A. Puretzky, L. Liang, X. Li, K. Xiao, B. G. Sumpter, V. Meunier and D. B. Geohegan, Twisted $MoSe_2$ Bilayers with Variable Local Stacking and Interlayer Coupling Revealed by Low-Frequency Raman Spectroscopy, *ACS Nano*, 2016, **10**, 2736–2744.

57 J. Xia, J. Yan and Z. X. Shen, Twisted MoSe2 Bilayers with Variable Local Stacking and Interlayer Coupling Revealed by Low-Frequency Raman Spectroscopy, *FlatChem*, 2017, **4**, 1–19.

58 R. Frisenda, Y. Niu, P. Gant, A. J. Molina-Mendoza, R. Schmidt, R. Bratschitsch, J. Liu, L. Fu, D. Dumcenco, A. Kis, D. Perez De Lara and A. Castellanos-Gomez, Micro-reflectance and transmittance spectroscopy: a versatile and powerful tool to characterize 2D materials, *J. Phys. D:Appl. Phys.*, 2017, **50**, 074002, DOI: 10.1088/1361-6463/AA5256.

59 K. F. Mak, C. Lee, J. Hone, J. Shan and T. F. Heinz, Atomically Thin MoS_2: A New Direct-Gap Semiconductor, *Phys. Rev. Lett.*, 2010, **105**, 136805, DOI: 10.1103/PhysRevLett.105.136805.

60 A. Splendiani, L. Sun, Y. Zhuang, T. Li, J. Kim, C.-Y. Chim, G. Galli and F. Wang, Emerging Photoluminescence in Monolayer MoS_2, *Nano Lett.*, 2010, **10**, 1271–1275, DOI: 10.1021/nl903868w.

61 M. Selig, G. Berghauser, A. Raja, P. Nagler, C. Schuller, T. F. Heinz, T. Korn, A. Chernikov, E. Malic and A. Knorr, *Nat. Commun.*, 2016, **7**, 13279, DOI: 10.1038/ncomms13279.

62 D. Christiansen, M. Selig, G. Berghäuser, R. Schmidt, I. Niehues, R. Schneider, A. Arora, S. Michaelis de Vasconcellos, R. Bratschitsch, E. Malic and A. Knorr, Phonon Sidebands in Monolayer Transition Metal Dichalcogenides, *Phys. Rev. B*, 2017, **119**, 187402, DOI: 10.1103/PhysRevLett.119.187402.

63 G. Antonius and S. G. Louie, Theory of exciton-phonon coupling, *Phys. Rev. B*, 2022, **105**, 085111, DOI: 10.1103/PhysRevB.105.085111.

64 L. Ortenzi, L. Pietronero and E. Cappelluti, Zero-point motion and direct-indirect band-gap crossover in layered transition-metal dichalcogenides, *Phys. Rev. B*, 2018, **98**, 195313, DOI: 10.1103/PhysRevB.98.195313.

65 S. Zheng, L. X. Sun, F. Zhou, F. Liu, Z. Liu, Z. Shen and H. J. Fan, Coupling and Interlayer Exciton in Twist-Stacked WS_2 Bilayers, *Adv. Opt. Mater.*, 2015, **3**, 1600–1605, DOI: 10.1002/adom.201500301.

66 W. Zhao, R. M. Ribeiro, M. Toh, A. Carvalho, C. Kloc, A. H. Castro Neto and G. Eda, Origin of Indirect Optical Transitions in Few-Layer MoS_2, WS_2, and WSe_2, *Nano Lett.*, 2013, **13**, 5627–5634, DOI: 10.1021/nl403270k.

67 O. Çakıroğlu, J. O. Island, Y. Xie, R. Frisenda and A. Castellanos-Gomez, An Automated System for Strain Engineering and Straintronics of 2D Materials, *Adv. Mater. Technol.*, 2023, **8**, 2201091, DOI: 10.1002/admt.202370005.